Innovation Series https://www.innoseries.com

An Improved Artificial Potential Field Method for Local Obstacle-Avoidance Path Planning of Intelligent Vehicles

Chaojie Lei, Wen Li*, Hongbing Chen, Yidan Gao, Hanlu Shi
Business School, East China University of Political Science and Law, Shanghai 201620, China
Corresponding Author: Wen Li (1609151361@qq.com)

Abstract: Aiming at the inherent defects of the traditional Artificial Potential Field (APF) method in local obstacle avoidance path planning for intelligent vehicles, including the Goal Non-Reachable with Obstacles Nearby (GNRON) problem, local minima traps, and path oscillation near obstacles, this paper proposes an improved APF method. The improvements include three aspects: introducing a relative distance factor to reconstruct the repulsive potential field function so that the repulsive force naturally vanishes at the goal position; designing a virtual sub-goal guidance strategy that generates a temporary sub-goal in the gradient-perpendicular direction when the vehicle is detected to be trapped in a local minimum; and constructing an adaptive step-size mechanism that dynamically adjusts the motion step according to obstacle proximity. Comparative experiments are conducted in six typical simulation scenarios with 50 independent trials each. Results show that the improved algorithm achieves 100% goal reachability across all scenarios, while the traditional APF completely fails in three challenging scenarios (GNRON, U-trap, symmetric obstacles) and only succeeds in three simpler ones. In the complex comprehensive scenario, path length is reduced by 5.5% and path smoothness is improved by 32.9%. The adaptive step-size strategy reduces path length by 23.5% and improves smoothness by 28.6% compared to fixed step sizes. Parameter sensitivity analysis demonstrates that 96.7% of parameter combinations yield successful path planning, indicating strong robustness.

Keywords: Artificial Potential Field; Path Planning; Local Obstacle Avoidance; Local Minima; Adaptive Step Size; Intelligent Vehicle

1. Introduction

1.1 Research Background and Significance

Path planning is essential for autonomous navigation in intelligent vehicles. Global methods, such as A* and Dijkstra's algorithm, require complete map information and are mainly suitable for known static environments, whereas local methods use online sensor information and are more appropriate for dynamic or partially unknown environments [1,2,15]. Among local methods, the Artificial Potential Field method (APF) is attractive because of its simple formulation, low computational cost, and real-time capability [1,3,4]. However, traditional APF suffers from goal non-reachability near obstacles, local-minimum trapping, and path oscillation, which limit its application in complex environments [5,8]. This study therefore develops an integrated APF improvement addressing all three limitations.

1.2 Research Status at Home and Abroad

Existing APF improvements mainly address GNRON, local minima, and path oscillation. Goal-distance factors and modified potential functions have been proposed for GNRON [5–7]. Detection criteria, virtual sub-goals, danger indices, and virtual walls have been used to escape local minima [8–11,19]. Modified repulsive fields and global–local integration have also been investigated to improve path quality [3,12–14]. However, most existing studies address only one limitation at a time. This paper therefore integrates a reconstructed repulsive field, deterministic virtual sub-goal guidance, and adaptive step-size control into a unified framework.

1.3 Main Work and Contributions of This Paper

The main contributions are as follows: (1) a goal-distance-weighted repulsive field with convergence analysis for the GNRON problem; (2) a deterministic gradient-perpendicular sub-goal strategy for local-minimum escape; (3) an obstacle-distance-based adaptive step-size mechanism for oscillation suppression; and (4) integration and validation of the three components in six simulation scenarios.

2. Traditional Artificial Potential Field Method and Its Problem Analysis

2.1 Basic Principles of the Artificial Potential Field Method

The Artificial Potential Field method abstracts the robot's motion space as a virtual potential field, in which the robot moves from the starting point to the target point under the action of the resultant force of the potential field. Let $\boldsymbol{q} \in R^2$ denote the current robot position, $\boldsymbol{q}_{goal} \in R^2$ the goal position, and $\mathbf{q}_{\mathrm{obs},i} \in \mathrm{R}^2$ the center of the ith obstacle.

The attractive potential field function is defined as:

$$U_{att}(q) = \frac{1}{2}k_{att}\rho^2\left(q, q_{goal}\right) \tag{1}$$

Where att denotes the attractive gain coefficient, and $\rho(q, q_{goal}) = \|q - q_{goal}\|$ represents the Euclidean distance from the robot to the target. The attractive force is defined as the negative gradient of the potential field:

$$F_{att}(q) = -\nabla U_{att}(q) = -k_{att}(q - q_{goal}) \tag{2}$$

As shown in Eq. (2), the direction of the attractive force always points toward the target, and its magnitude is proportional to the distance from the robot to the target. When the robot is far from the target, the attractive force is relatively large; as the robot approaches the target, the attractive force gradually tends to zero.

The traditional repulsive potential field function is defined as:

$$U_{rep}(q) = \frac{1}{2}k_{rep}\left(\frac{1}{\rho(q, q_{obs})} - \frac{1}{\rho_0}\right)^2, \rho(q, q_{obs}) \le \rho_0 \tag{3}$$

When $\rho(q, q_{obs}) > \rho_0$, $U_{rep}(q) = 0$. Here, rep denotes the repulsive gain coefficient, $\rho(q, q_{obs})$ represents the shortest distance from the robot to the obstacle, and ρ_0 denotes the obstacle influence radius. Taking the gradient of Eq. (3) yields the repulsive force:

$$F_{rep}(q) = k_{rep}\left(\frac{1}{\rho(q, q_{obs})} - \frac{1}{\rho_0}\right)\frac{1}{\rho^2(q, q_{obs})}\nabla\rho(q, q_{obs}) \tag{4}$$

Driven by the resultant force $F(q) = F_{att}(q) + \sum_i F_{rep,i}(q)$, the robot moves iteratively. At each step, it advances along the direction of the resultant force with a fixed step size δ, until it reaches the target or the maximum number of iterations is reached.

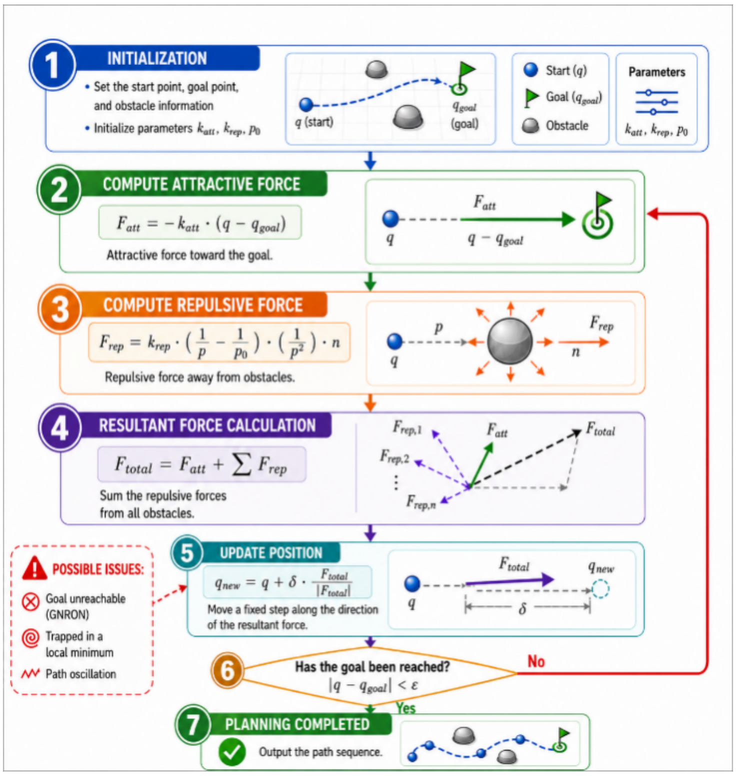

Figure 1: Basic flowchart of the traditional APF algorithm.

As shown in Figure 1, the traditional APF algorithm iteratively calculates the attractive and repulsive forces and moves the robot along the resultant-force direction. Its computational complexity per iteration is $O(M)$, where $M$is the number of obstacles. Despite its efficiency, the method suffers from three inherent limitations.

2.2 Analysis of the Goal Non-Reachable Problem

When obstacles are located near the target point ($\rho(q_{goal}, q_{obs}) < \rho_0$), the attractive force decreases according to Eq. (2) as the robot approaches the target, whereas the repulsive force remains relatively large according to Eq. (4). When the repulsive force is greater than the attractive force, the direction of the resultant force deviates from the target, causing the robot to repeatedly wander near the target and fail to reach it.

From a mathematical perspective, when $q \to q_{goal}$, $\|F_{att}\| = k_{att}\rho(q, q_{goal}) \to 0$. However, if $\rho(q_{goal}, q_{obs}) < \rho_0$, then $\|F_{rep}\| > 0$. As a result, the resultant force at the target point is nonzero and its direction deviates from the target. The root cause of this problem is that the traditional repulsive force function is independent of the distance to the target and lacks a coordination mechanism with the navigation objective.

2.3 Analysis of the Local Minima Problem

A local minimum refers to a non-target equilibrium point in the potential field, namely $F(q^*) = 0$ but $q^* \neq q_{goal}$. A typical scenario is a region enclosed by U-shaped obstacles: after the robot enters the interior of the U-shaped structure, the repulsive force generated by the bottom wall and the attractive force reach equilibrium at a certain point, resulting in a zero resultant force and causing the robot to stagnate. Assume that the U-shaped structure consists of a left wall, a bottom wall, and a right wall.

The bottom wall generates a backward repulsive force, while the lateral repulsive forces from the left and right walls cancel each other out due to symmetry. When $\|F_{rep,bottom}\| = \|F_{att}\|$, a stable equilibrium is formed. A similar problem also occurs in environments with symmetrically distributed obstacles: the lateral repulsive forces from obstacles on both sides cancel each other out, while the longitudinal forces reach equilibrium.

2.4 Analysis of the Path Oscillation Problem

In narrow passages, the obstacles on both sides of the robot are close to the robot, and the repulsive forces from the left and right sides alternately dominate, causing the direction of the resultant force to switch repeatedly. When the fixed step size is too large, the displacement may exceed the safe range of the passage, resulting in zigzag oscillations. Experimental data show that a large fixed step size (0.5m) leads to planning failure in complex environments, with a success rate of 0%, whereas a small fixed step size (0.1m) allows the robot to pass through but increases the path length by more than 30%.

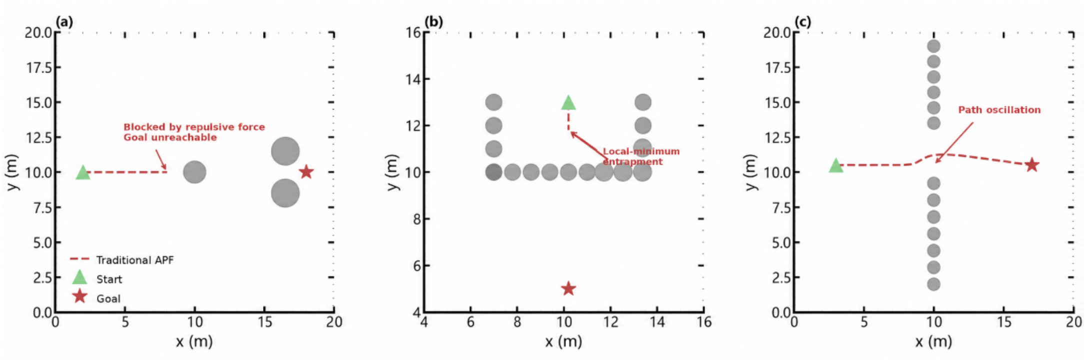

Figure 2: Schematic illustration of the three major defects of the traditional APF method.

Figure 2 illustrates the three typical defects of the traditional APF method: goal non-reachability, local-minimum trapping, and path oscillation. These problems limit its applicability in complex environments.

3. Improved Artificial Potential Field Method

3.1 Improved Repulsive Potential Field Function

To solve the goal non-reachable problem, this paper introduces a relative distance factor between the robot and the target based on the Ge-Cui method [5] to reconstruct the repulsive potential field function. The core idea of the Ge-Cui method is to make the repulsive force positively correlated with the distance to the target. This paper adopts its mathematical framework and selects n=2 as the distance-factor exponent:

$$U'_{rep}(q) = \frac{1}{2}k_{rep}\left(\frac{1}{\rho(q,q_{obs})} - \frac{1}{\rho_0}\right)^2 \cdot \rho^n(q,q_{goal}), \rho(q,q_{obs}) \le \rho_0 \tag{5}$$

When $\rho(q,q_{obs}) > \rho_0$, $U'_{rep}(q) = 0$. Here, $\rho^n(q,q_{goal})$ denotes the relative distance factor, with $n = 2$ This factor makes the repulsive potential energy positively correlated with the distance from the robot to the target: when $\rho(q,q_{goal}) \to 0$, $U'_{rep} \to 0$, and the repulsive force naturally vanishes.

Unlike the original Ge-Cui formulation, the proposed framework further incorporates local-minimum escape and adaptive step-size control.

Taking the gradient of the improved repulsive potential field yields two components:

$$F'_{rep}(q) = F_{rep1}(q) + F_{rep2}(q) \tag{6}$$

The first component acts in the direction away from the obstacle:

$$F_{rep1}(q) = k_{rep}\left(\frac{1}{\rho(q,q_{obs})} - \frac{1}{\rho_0}\right)\frac{\rho^n(q,q_{goal})}{\rho^2(q,q_{obs})}\nabla\rho(q,q_{obs}) \tag{7}$$

The second component points toward the target:

$$F_{rep2}(q) = -\frac{n}{2}k_{rep}\left(\frac{1}{\rho(q,q_{obs})} - \frac{1}{\rho_0}\right)^2 \rho^{n-1}(q,q_{goal})\nabla\rho(q,q_{goal}) \tag{8}$$

Theorem 1 (Convergence at the target point): When $n \geq 2$, the improved repulsive force $F'_{rep}(q)$ is strictly zero at the target point $goal$.

Proof: When $q \to q_{goal}$, $\rho(q,q_{goal}) \to 0$.

For $rep1$ in Eq. (7), the factor $\rho^n(q,q_{goal})$ tends to zero as $q \to q_{goal}$, while $(\frac{1}{\rho(q,q_{obs})} - \frac{1}{\rho_0})\frac{1}{\rho^2(q,q_{obs})}$ remains bounded near the target under the prerequisite that the target and the obstacle do not coincide, namely $\rho(q_{goal},q_{obs}) > 0$. Therefore, $F_{rep1} \to 0$.

For $rep2$ in Eq. (8), when $n = 2, \rho^{n-1}(q,q_{goal}) = \rho(q,q_{goal}) \to 0$. Regarding the issue that $\nabla\rho(q,q_{goal}) = \frac{q-q_{goal}}{\|q-q_{goal}\|}$ is undefined at $q = q_{goal}$, it should be noted that the product $\rho^{n-1}\nabla\rho = \rho(q,q_{goal}) \cdot \frac{q-q_{goal}}{\|q-q_{goal}\|} = q - q_{goal} \to 0$ tends to the zero vector in vector value. Therefore, $F_{rep2} \to 0$.

When $n > 2, \rho^{n-1} \to 0$ has a faster convergence rate $O(\|q - q_{goal}\|^{n-1})$, indicating stronger convergence.

In summary, at the target point, the resultant force is determined only by the attractive force $F'_{rep} = F_{rep1} + F_{rep2} = 0$, $F_{att} \to 0$, and the robot is in a stable equilibrium state at the target point.

It should be noted that the above proof requires that the target and the obstacle do not coincide, namely $\rho(q_{goal},q_{obs}) > 0$. In practical applications, this condition is always satisfied.

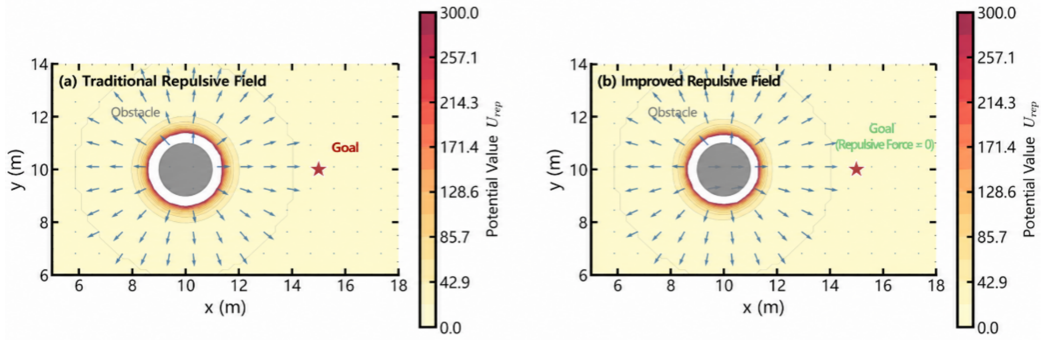

Figure 3: Comparison of the Repulsive Force Field Before and After Improvement.

Figure 3 shows that the traditional field retains nonzero repulsion near the goal, whereas the improved field makes the repulsive force vanish at the goal while preserving obstacle-avoidance capability elsewhere.

3.2 Virtual Sub-goal Escape Strategy

This paper designs a deterministic escape strategy: when a local minimum is detected, a virtual sub-goal is generated to guide the robot around the trap.

A local minimum is detected when the accumulated displacement over $K = 10$ consecutive steps is smaller than the trap threshold $\varepsilon_{\text{trap}}$:

$$\sum_{t=t_0}^{t_0+K} \left\| q_{t+1} - q_t \right\| < \epsilon_{trap} \tag{9}$$

Where $\epsilon_{trap} = K \cdot \delta_{min} \cdot 0.1 = 0.1$m, indicating that the accumulated displacement is less than 10% of the minimum step size, which means that the robot is essentially stagnant.

After a trap is detected, the direction of the resultant force is calculated at the current position, and a sub-goal is generated in the perpendicular direction:

$$q_{sub} = q_{trap} + d_{sub} \cdot g^{\wedge}_{\perp} \tag{10}$$

Where $g^{\wedge}_{\perp}$ is the vector obtained by rotating $g^{\wedge}$clockwise by 90 degrees. If an obstacle exists within the range of this direction, the counterclockwise direction is selected instead, ensuring that the sub-goal lies outside the obstacle influence range. Here, $d_{\text{sub}} = 1.5\rho_0$. After it is generated, the sub-goal temporarily replaces $\mathbf{q}_{\text{goal}}$ in the resultant-force calculation. Once the robot reaches the sub-goal or leaves the trap region, the original goal is restored. The maximum number of escape steps is set to $N_{\text{esc}} = 200$ to prevent infinite loops.

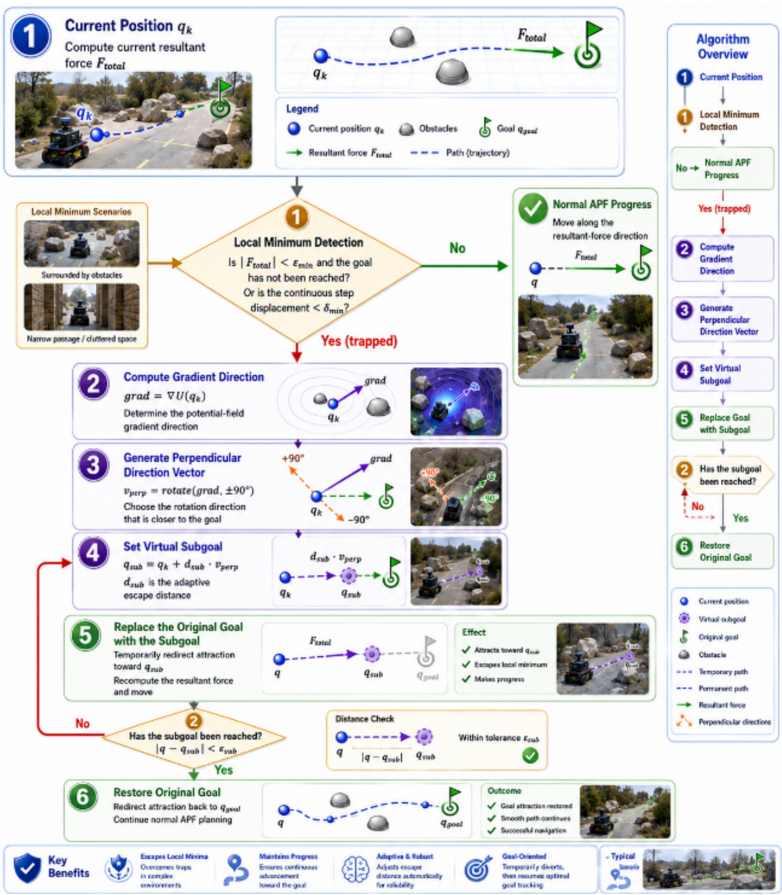

Figure 4: Flowchart of the virtual sub-goal escape strategy.

Figure 4 summarizes the deterministic virtual sub-goal escape procedure.

3.3 Adaptive Step-size Mechanism

This paper constructs an adaptive step-size mechanism associated with the distance to obstacles:

$$\delta(q) = \delta_{min} + (\delta_{max} - \delta_{min}) \cdot min\left(\frac{\rho_{min}(q)}{\rho_0}, 1\right) \tag{11}$$

Where $\delta_{\min} = 0.1$ m, $\delta_{\max} = 0.5$ m, and $\rho_{\min}(\mathbf{q})$denotes the distance to the nearest obstacle. When $\rho_{\min} \geq \rho_0$, the step size is $\delta_{\max}$, enabling efficient passage; as $\rho_{\min} \to 0$, it approaches $\delta_{\min}$, allowing fine control near obstacles. The linear transition preserves path continuity and suppresses oscillation.

Compared with the fixed 0.1 m step, the adaptive strategy reduced the path length and turning-angle sum by 23.5% and 28.6%, respectively, whereas the fixed 0.5 m step failed.

3.4 Overall Workflow of the Improved Algorithm

The execution process integrating the three improvements is as follows:

Algorithm 1: Improved Artificial Potential Field Method

Input: start position $\mathbf{q}_0$, goal position $\mathbf{q}_{\text{goal}}$, obstacle set $\{\mathbf{q}_{\text{obs},i}\}$, and parameters $k_{\text{att}}, k_{\text{rep}}, \rho_0, \delta_{\min}, \delta_{\max}, n$

Output: planned path $Q = \{\mathbf{q}_0, \mathbf{q}_1, \dots, \mathbf{q}_T\}$.

1. Initialize: $q \leftarrow q_0$, $target \leftarrow q_{goal}$, $trapped$ ←false, $count \leftarrow 0$

2. while $\rho(q, q_{goal}) > d_{goal}$ and $count < N_{max}$ do

3. \quad if a local minimum is detected according to Eq. (9) then

4. \quad\quad Generate a sub-goal according to Eq. (10); $target \leftarrow \mathbf{q}_{\text{sub}}$; $trapped \leftarrow true$

5. \quad else if $trapped = true$ and (the sub-goal has been reached or the trap region has been exited) then

6. \quad\quad $trapped \leftarrow false$

7. \quad end if

8. \quad Calculate $F_{att}(q)$ (according to Eq. (2), with the attractive force pointing toward *target*)

9. \quad Calculate $\mathbf{F}_{\text{rep}}$according to Eqs. (6)–(8), using $target$ in place of $\mathbf{q}_{\text{goal}}$

10. \quad $F \leftarrow F_{att} + \sum_i F'_{rep,i}$

11. \quad Calculate the adaptive step size according to Eq. (11)

12. \quad $q \leftarrow q + \delta(q) \cdot F$^

13. \quad $count \leftarrow count + 1$

14. end while

15. return Q

Figure 5: Overall architecture of the improved APF algorithm.

Figure 5 presents the overall architecture of the proposed method, which integrates the improved repulsive field, virtual sub-goal guidance, and adaptive step-size control. Its computational complexity is $O(TM)$, where T is the number of iterations and $M$is the number of obstacles, which is of the same order as that of the traditional APF method.

4. Simulation Experiments and Results Analysis

4.1 Simulation Environment and Parameter Settings

A two-dimensional simulation platform was developed using Python. The robot was modeled as a point robot, without considering its physical dimensions. Six typical scenarios were designed, and each scenario was repeated 50 times. The compared methods included the traditional APF, the improved APF, and RRT [16,17]. The same start and target points and obstacle configurations were used to ensure fairness. The evaluation metrics included goal reachability, path length, planning time, path smoothness, defined as the sum of turning angles, and the minimum safety distance.

RRT was included only as a global-planning benchmark because it assumes complete map information, whereas APF relies on local sensing. The 50 repetitions were used to measure runtime variation for the deterministic APF methods and path-statistic variation for the stochastic RRT method.

The simulation parameters are summarized in Table 1. For scenario S5, the start and goal positions were (1, 1)and (28, 28), respectively; the remaining scenarios used the configurations described below. The simulations were implemented in Python 3.10 with NumPy 1.24 on an Intel Core i7 processor.

Table 1: Simulation Experiment Parameter Settings.

Parameter	Symbol	Value	Unit
Attraction gain	*att*	5.0	—
Repulsion gain	*rep*	80.0	—
Obstacle influence radius	ρ_0	3.0	m

Distance factor exponent	n	2	—
Adaptive step-size range	δ	[0.1, 0.5]	m
Maximum number of iterations	max	3000	—
Goal-reaching threshold	$goal$	0.5	m
Trap-detection window	K	10	steps
Trap-detection threshold	$trap$	0.5	m
Subgoal distance	sub	$1.5\rho_0$= 4.5	m
Maximum escape steps	esc	200	—
Number of repetitions per scenario	—	50	times

Note: The parameter values were determined based on the results of the parameter sensitivity analysis, as detailed in Section 4.6.

The six scenarios were designed as follows: S1, a simple open environment, 20 × 20 m with 5 obstacles; S2, a goal non-reachable environment, with 4 obstacles near the target; S3, a U-shaped trap, formed by 16 obstacles; S4, a narrow passage, formed by 16 obstacles arranged as parallel passages with a passage width of 4 m; S5, a complex comprehensive environment, 30 × 30 m with 12 mixed obstacles; and S6, a symmetric-obstacle environment, with 5 symmetrically distributed obstacles.

4.2 Verification of the Goal Non-Reachable Scenario

In scenario S2, the target is tightly surrounded by four obstacles ($\rho(q_{goal}, q_{obs}) < \rho_0$). The traditional APF has a success rate of 0%, because the repulsive force at the target is always greater than the attractive force. In contrast, the improved APF achieves a success rate of 100%, because the distance factor causes the repulsive force to decay to zero near the target.

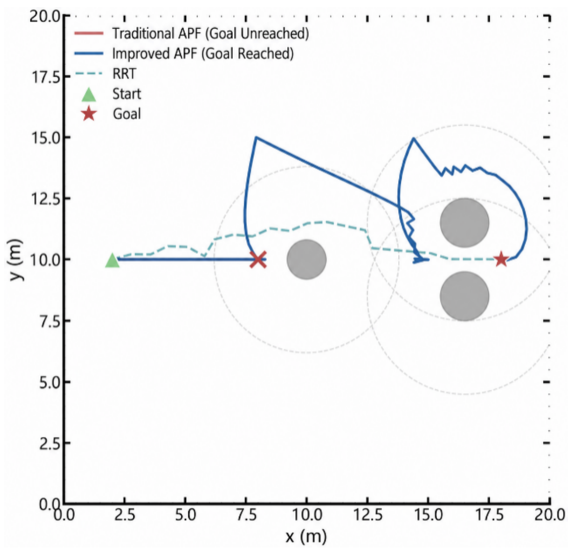

Figure 6: Path comparison in the goal non-reachable scenario.

As shown in Figure 6 and Table 2, the improved APF successfully reaches the goal, whereas the traditional APF fails. RRT produces a shorter path because it uses complete global-map information, while the improved APF maintains a larger obstacle-clearance margin.

4.3 Verification of Local Minimum Escape

In the S3, U-shaped trap, and S6, symmetric-obstacle, scenarios, the traditional APF completely fails, with a success rate of 0%, whereas the improved APF achieves a success rate of 100% in both scenarios.

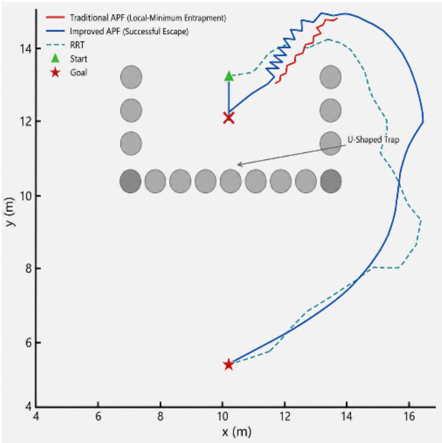

Figure 7: Path comparison for local minimum escape.

Figure 7 shows that the traditional APF stagnates at the force-equilibrium point in the U-shaped scenario, whereas the improved APF generates a virtual sub-goal and successfully escapes the trap. Table 2 further shows that the deterministic clockwise rule also enables successful escape in the S6 symmetric-obstacle scenario. The improved APF succeeds in both scenarios.

4.4 Verification of Path Oscillation Suppression

In the S4 narrow-passage scenario, all three methods succeed. Because the passage is relatively wide, the difference between the traditional and improved APF methods is limited.

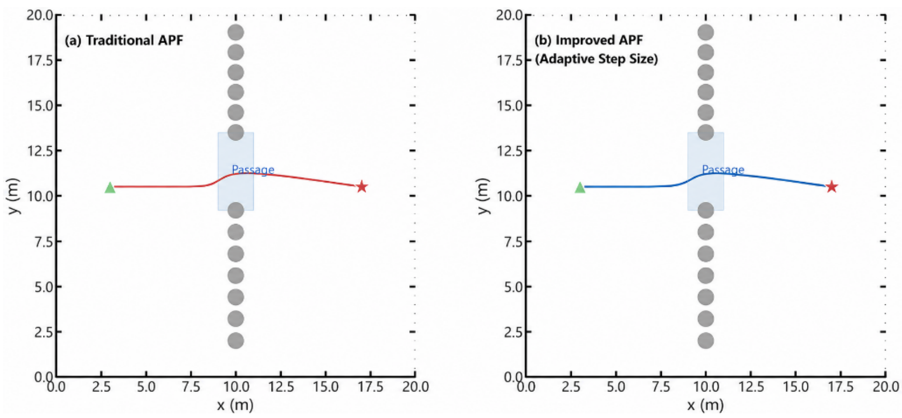

Figure 8: Comparison of Path Oscillation in the Narrow-passage Scenario.

Figure 8 shows that the adaptive step-size mechanism slightly reduces directional jitter in the narrow passage. Its advantage is more evident in S5, where the turning-angle sum decreases by 32.9% and the path length decreases by 5.5%.

4.5 Comprehensive Performance Comparison

The S5 complex comprehensive environment, 30 × 30 m with 12 mixed obstacles, comprehensively tests the capability of the algorithms. All three methods succeed in this scenario, with a success rate of 100%.

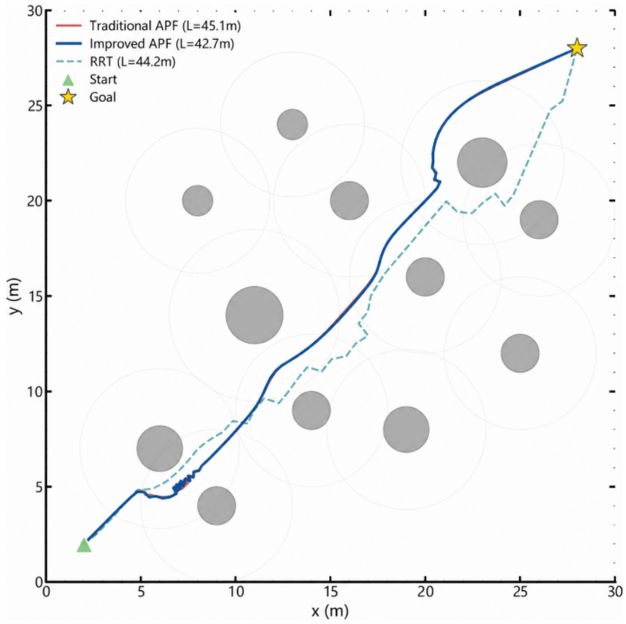

Figure 9: Path comparison of multiple methods in the comprehensive environment.

Figure 9 shows that the adaptive mechanism uses smaller steps near obstacles and larger steps in open regions, producing a more compact path. The quantitative results for all six scenarios are summarized in Table 2.

Table 2: Comprehensive Performance Comparison of Multiple Methods Across Multiple Scenarios.

Scenario	Method	Success Rate (%)	Path Length (m)	Planning Time (ms)	Smoothness (rad)	Minimum Safety Distance (m)
Simple Open Environment (S1)	Traditional APF	100	25.46 ± 0.00	5.02 ± 1.02	0.00	5.76
Simple Open Environment (S1)	Improved APF	100	25.46 ± 0.00	4.42 ± 0.88	0.00	5.77
Simple Open Environment (S1)	RRT	100	29.31 ± 1.02	13.47 ± 3.98	17.37 ± 3.21	3.72
GNRON (S2)	Traditional	0	—	—	—	—

GNRON (S2)	APF Improved APF	100	43.11 ± 0.00	12.73 ± 1.43	93.55 ± 0.00	0.91
GNRON (S2)	RRT	100	20.58 ± 3.27	28.22 ± 38.73	14.14 ± 4.26	0.38
U-shaped Trap (S3)	Traditional APF	0	—	—	—	—
U-shaped Trap (S3)	Improved APF	100	27.69 ± 0.00	24.00 ± 1.93	68.11 ± 0.00	1.13
U-shaped Trap (S3)	RRT	100	22.30 ± 3.15	25.34 ± 13.12	15.07 ± 4.72	0.82
Narrow Passage (S4)	Traditional APF	100	14.19 ± 0.00	3.74 ± 0.64	1.22 ± 0.00	1.45
Narrow Passage (S4)	Improved APF	100	14.18 ± 0.00	5.28 ± 0.55	1.21 ± 0.00	1.46
Narrow Passage (S4)	RRT	100	16.77 ± 1.02	8.27 ± 10.16	11.45 ± 2.39	0.75
Composite Scenario (S5)	Traditional APF	100	45.13 ± 0.00	12.82 ± 1.01	77.28 ± 0.00	0.86
Composite Scenario (S5)	Improved APF	100	42.66 ± 0.00	17.02 ± 1.15	51.89 ± 0.00	0.82
Composite Scenario (S5)	RRT	100	44.18 ± 1.72	42.14 ± 20.11	27.67 ± 3.91	0.35
Symmetric Scenario (S6)	Traditional APF	0	—	—	—	—
Symmetric Scenario (S6)	Improved APF	100	26.94 ± 0.00	8.48 ± 0.87	32.99 ± 0.00	1.12
Symmetric Scenario (S6)	RRT	100	21.34 ± 1.55	8.69 ± 3.33	15.13 ± 3.39	0.61

Note: Values are presented as mean ± standard deviation over 50 trials; "—" denotes planning failure. Smoothness is measured by the sum of turning angles, with lower values indicating smoother paths. APF paths are deterministic; therefore, their path-related standard deviations are zero.

As summarized in Table 2, the improved APF achieved 100% success in all six scenarios, whereas the traditional APF failed in S2, S3, and S6. In S5, the proposed method reduced the path length and smoothness metric by 5.5% and 32.9%, respectively. It also maintained millisecond-level planning time and generally provided a larger safety margin than RRT.

4.6 Parameter Sensitivity Analysis

In scenario S5, a grid search was conducted for $k_{att} \in \{1,2,3,5,7,10\}$ and $k_{rep} \in \{50,80,100,150,200\}$, resulting in 30 parameter combinations.

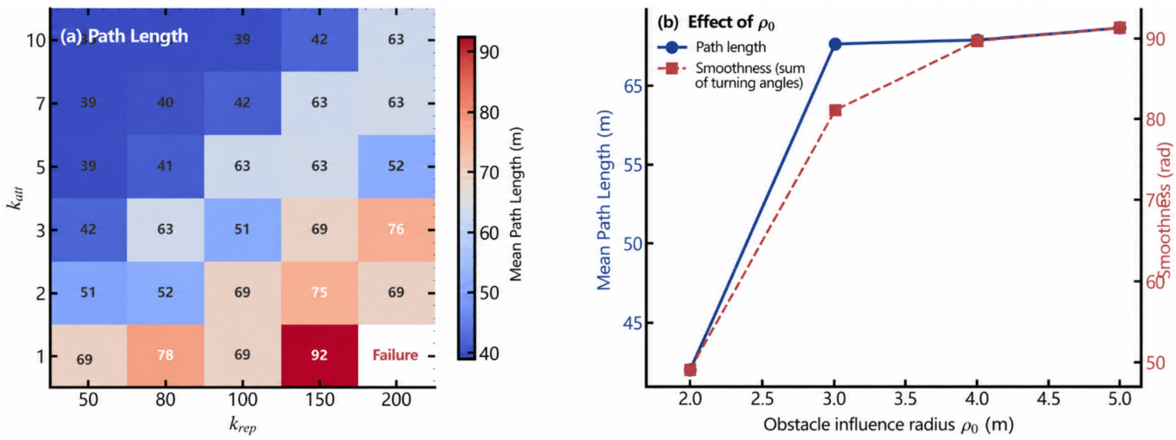

Figure 10: Parameter sensitivity analysis.

Figure 10 shows that 29 of the 30 gain-coefficient combinations, accounting for 96.7%, produced successful paths. The only failure occurred when the attractive force was excessively weak relative to the repulsive force. For obstacle influence radii from 2.0 to 5.0 m, the success rate remained 100%, although the path length increased with the influence radius because the robot began detouring earlier. These results demonstrate stable performance over a broad parameter range.

4.7 Robustness Test

Two robustness tests were conducted. Across 100 random-obstacle trials, the improved APF achieved a success rate of 95%, compared with 75% for the traditional APF and 100% for RRT; the failures occurred only when dense obstacles blocked all feasible passages. Under Gaussian obstacle-position noise in S5, the improved APF maintained a success rate of 100%, with path lengths ranging from 42.66 to 52.28 m.

5. Discussion

5.1 Limitations and Applicable Conditions

Although the results confirm the complementary effects of the three proposed components, the method still has three main limitations. First, as a local planner, it may fail in extremely dense environments and may generate longer paths than global methods because it lacks complete environmental information. Second, the current point-robot model is limited to two-dimensional static environments and does not consider vehicle dimensions, kinematic constraints, sensor limitations, or dynamic-obstacle prediction. Third, although the method is relatively insensitive to parameter variations, parameter selection remains empirical and extreme gain ratios may cause failure. Practical deployment therefore requires obstacle inflation, kinematic-feasibility checks, dynamic perception, and preferably online parameter adaptation.

5.2 Future Work

Future work will extend the method to dynamic and three-dimensional environments, integrate global guidance with local APF control, develop online parameter adaptation, and validate the algorithm on a physical intelligent-vehicle platform equipped with real-time LiDAR.

6. Conclusion

This paper proposed an improved APF framework combining a goal-distance-weighted repulsive field, deterministic virtual sub-goal guidance, and adaptive step-size control. The proposed method reached the goal in all six representative scenarios, resolving the GNRON, U-shaped-trap, and symmetric-obstacle failures of traditional APF. In the comprehensive scenario, it reduced the path length by 5.5% and the turning-angle sum by 32.9%. It also maintained millisecond-level planning time, succeeded for 96.7% of the tested parameter combinations, achieved 95% success in random-obstacle environments, and remained successful under obstacle-position noise. These results demonstrate that the proposed method improves reliability and path quality while retaining low computational complexity.

Acknowledgment

This study was supported by the Innovation and Entrepreneurship Training Program for Undergraduates of Yingkou Institute of Technology under Grant No. S202514435027 (Project Title: Design of Intelligent Car Based on Single-Chip Microcomputer).

References

[1] Khatib O. Real-time obstacle avoidance for manipulators and mobile robots[J]. International Journal of Robotics Research, 1986, 5(1): 90-98.

[2] Fox D, Burgard W, Thrun S. The dynamic window approach to collision avoidance[J]. IEEE Robotics & Automation Magazine, 1997, 4(1): 23-33.

[3] Zhou Z, Chen J. Semantic-aware path planning with A* and APF integration for complex environments[J]. Robotics and Autonomous Systems, 2023, 160: 104325.

[4] Ge S S, Cui Y J. Dynamic motion planning for mobile robots using potential field method[J]. Autonomous Robots, 2002, 13(3): 207-222.

[5] Ge S S, Cui Y J. New potential functions for mobile robot path planning[J]. IEEE Transactions on Robotics and Automation, 2000, 16(5): 615-620.

[6] Park M G, Jeon J H, Lee M C. Obstacle avoidance for mobile robots using artificial potential field approach with simulated annealing[C]// IEEE International Symposium on Industrial Electronics. Pusan: IEEE, 2001: 1530-1535.

[7] Luo G, Yu L, Pourcel L. A reliable path planning algorithm based on adjustable radius virtual circle model[J]. Journal of Intelligent & Robotic Systems, 2021, 103(2): 1-16.

[8] Koren Y, Borenstein J. Potential field methods and their inherent limitations for mobile robot navigation[C]// IEEE International Conference on Robotics and Automation. Sacramento: IEEE, 1991: 1398-1404.

[9] Liu Zhijie, Zhang Minglu, Zhang Xiaojun. Path planning of mobile robots based on an improved artificial potential field method[J]. robot, 2018, 40(1): 24-30.

[10] Li G, Yamashita A, Asama H, et al. An efficient improved artificial potential field based regression search method for robot path planning[C]// IEEE International Conference on Mechatronics and Automation. Chengdu: IEEE, 2012: 1227-1232.

[11] Sun J, Liu G, Tian G, et al. Smart obstacle avoidance using a danger index for a dynamic environment[J]. Applied Sciences, 2019, 9(8): 1589.

[12] Rostami S M H, Sangaiah A K, Wang J, et al. Obstacle avoidance of mobile robots using modified artificial potential field algorithm[J]. EURASIP Journal on Wireless Communications and Networking, 2019, 2019(1): 1-19.

[13] Cai Zixing, He Hangen, Chen Hong. Current status and future development of mobile robot technology research[J]. robot, 2002, 24(5): 475-480.

[14] Montiel O, Orozco-Rosas U, Sepulveda R. Path planning for mobile robots using bacterial potential field for avoiding static and dynamic obstacles[J]. Expert Systems with Applications, 2015, 42(12): 5177-5191.

[15] Mac T T, Copot C, Tran D T, et al. Heuristic approaches in robot path planning: a survey[J]. Robotics and Autonomous Systems, 2016, 86: 13-28.

[16] LaValle S M. Rapidly-exploring random trees: a new tool for path planning[R]. Computer Science Department, Iowa State University, 1998.

[17] Karaman S, Frazzoli E. Sampling-based algorithms for optimal motion planning[J]. International Journal of Robotics Research, 2011, 30(7): 846-894.

[18] Zhang Tao, Li Qingdu. Mobile robot path planning based on an improved RRT algorithm[J]. Computer Engineering and Applications, 2019, 55(12): 234-239.

[19] Weerakoon T, Ishii K, Nassiraei A A F. An artificial potential field based mobile robot navigation method to prevent from deadlock[J]. Journal of Artificial Intelligence and Soft Computing Research, 2015, 5(3): 189-203.

[20] Zhao Dongbin, Liu Derong, Yi Jianqiang. A review of path planning methods based on deep reinforcement learning[J]. Control and Decision, 2021, 36(7): 1521-1536.